Journal of Radioanalytical and Nuclear Chemistry (2018) 316:1337–1346
https://doi.org/10.1007/s10967-018-5839-8

Interaction of Eu(III) on magnetic biochar investigated by batch, spectroscopic and modeling techniques

Yuling Zhu[1] · Cong Zheng[1] · Siying Wu[1] · Yuanzhi Song[1] · Baowei Hu[1]

Received: 20 December 2017 / Published online: 28 March 2018

Abstract
Interaction mechanism of Eu(III) on magnetic biochar(MB) was investigated by batch, XPS, EXAFS and modeling techniques. Maximum Eu(III) adsorption capacity on MB is 105.53 mg/g at pH 3.0, which was demonstrated to various functional groups by XPS analysis. No effect of ionic strength revealed inner-sphere surface complexation. According to EXAFS analysis, inner-sphere surface complexation and surface co-precipitation dominated the Eu(III) adsorption at low and high pH, respectively. Eu(III) adsorption can be simulated by surface complexation modeling. These results indicated that MB can be used a promising candidate for the highly effective adsorbent of radionuclides.

Keywords Radionuclides · Spectroscopic analysis · Magnetic biochar · Modeling

Introduction

Immoderate discharge of radionuclides during mining and processing processes has posed a serious threat to ecological environment and human health [1]. Therefore, much effort has been made to remove radionuclides before discharged into environments. Adsorption approach is a highly effective method to remove radionuclides from wastewater due to easy-operation, low-cost and environmentally friendly [2]. Eu(III) has been extensively used as a chemical analogue of trivalent actinides in recent years. The removal of Eu(III) on various adsorbents has been widely investigated such as clay minerals [3–6], Fe/Al-(hydr)oxides [7–10], and carbon-based materials [11–15]. Wang et al. elucidated the adsorption mechanism of Eu(III) on carbon nanotubes using batch, spectroscopy and theoretical calculation [16].

Biochar as a common carbon-based adsorbent, generally produced from the thermal or hydrothermal conversion of biomass, could significantly increase the removal of environmental pollutants through surface complexation due to the occurrence of various functional groups [17, 18]. In recent years, an alternative technology was developed to use engineered biochars (such as magnetic biochar) to remove various pollutants, including organics [19–23], Cr(VI) [24–26], Pb(II) [27–29] and arsenic [30–32]. For example, Yang et al. utilized magnetic biochar to remove Hg^0 from the simulated combustion flue gas [33]. Magnetic biochar can be easily separated from liquid phase by a magnet after adsorption experiments. In addition, magnetite of magnetic biochar presents the high redox potential (2–5 eV) over wide pH range [34]. However, limited investigation regarding adsorption mechanism of Eu(III) on magnetic biochar by spectroscopic and modeling techniques were reported by far.

In this study, magnetite nanoparticles anchored biochar was synthesized by fast pyrolysis of $FeCl_2$ pre-adsorbed biomass under N_2 conditions. The objectives of this study were (1) to synthesize magnetic biochar by a facile method and characterize them using SEM, TEM, FT-IR, XRD and XPS techniques; (2) to investigate the effect of water chemistry on Eu(III) adsorption on magnetic biochar by batch techniques; and (3) to determine interaction mechanism of Eu(III) on magnetic biochar by XPS, EXAFS and modeling techniques. The highlight of this manuscript was to apply biochar-based adsorbent in practical environmental cleanup.

Electronic supplementary material The online version of this article (https://doi.org/10.1007/s10967-018-5839-8) contains supplementary material, which is available to authorized users.

✉ Baowei Hu
hbw@usx.edu.cn

[1] School of Life Science, Shaoxing University, Huancheng West Road 508, Shaoxing 312000, People's Republic of China

Experimental

Materials

The rice straw is a common crop residue, which was collected from a farm near the suburb of Shaoxing, China. Ferrous chloride hexahydrate ($FeCl_2 \cdot 6H_2O$) and europium nitrate ($Eu(NO_3)_3$) of analytical grade were purchased from Sinopharm Chemical Reagent Co., Ltd and used as received. The deionized water (18.2 M, Nanopure water, Barnsead) was utilized in this study.

Synthesis of magnetic biochar

In this study, magnetic biochar was synthesized via thermal conversion of $FeCl_2$ pre-adsorbed rice straw under N_2 conditions. Briefly, the rice straw was firstly air-dried (moisture < 5%) and ground to 100 meshes. Then, 50 g of $FeCl_2$ and 100 g of biomass were added to 100 mL DI water under vigorous stirring. After pre-adsorption equilibrium (24 h), the mixture was centrifuged at 6000 rpm for 10 min and then was dried at 70 °C for 6 h under glovebox conditions. The Fe(II)-loaded biomass were placed in lab-scale stainless-steel pyrolysis reactor and then heated at a heating rate of 20 °C/min to achieve five settled gradient temperatures (200, 300, 400, 500 and 600 °C) under a N_2 atmosphere. The heating time at each gradient temperature was set 1 h to provide enough time for biomass carbonization and minimize volatile organic decompositions [35]. After cool to room temperature, the mixtures were gently crushed and sealed in a vacuum container before use.

Characterization of magnetic biochar

The microscopic morphology of as-prepared magnetic biochar was characterized by SEM (JEOL 6500F, Japan) equipped with an energy-dispersive X-ray analyzer and high resolution TEM (JEM-2010, Japan). FT-IR spectrometer (Thermo Nicolet IS10 Spectrometer, USA) was also used to identify the chemical functional groups in the range of 4000–400 cm^{-1} with a scan rate of 0.1 cm/s. Briefly, the sample was primarily freeze-dried for 24 h, and then ground with KBr powder (1:100) in an agate mortar. The disc was obtained by compressing it in a hydraulic press. The crystallographic mineralogy was identified by D/Max-IIIA Powder X-ray Diffractomer (Rigaku Corp., Japan) equipped with a graphite monochromator in the angular range from 5 to 60° with 0.02° of step size at 35 kV and 25 mA. Carbon, nitrogen, hydrogen content of biochar was analyzed by an element analyzer (Vario ELIII, Elementar, Germany). N_2-BET and pore size of magnetic biochar were measured by NOVA 4200e Surface area and Pore size analyzer (Quantachrome, FL, USA). The zeta potentials of magnetic biochar were conducted using Malvern Zetasizer Nano ZS.

Batch adsorption experiments

The batch triple experiments of Eu(III) (10 mg/L) adsorption on magnetic biochar (m/v = 1.2 g/L) were conducted at 10 mL of polycarbonate centrifuge tube at room temperature under glovebox conditions. Adsorption kinetics and isotherms were examined at pH 3.0 under different time (5–2880 min) and concentration in the range of 10–50 mg/L, respectively. Briefly, 12 mg magnetic biochar was added into 10 mL Eu(III) solution (60 mg/L) with 0.01 mol/L NaCl electrolyte, and then pH values were adjusted to 3.0 by adding neglected volume of NaOH/HCl solutions (0.1–1.0 mol/L). Then suspensions were reacted at ambient conditions at a 200 rpm thermostatic reciprocating shaker for 24 h. After adsorption, the solid phase was separated by a magnet and supernatant was filtered through 0.22 μm nylon membrane filters. The Fe concentration in the supernatant was analyzed by Z-500 flame atomic absorption spectrophotometer (FAAS, Hitachi, Japan). The Eu(III) concentration in supernatant was measured using inductively coupled plasma-mass spectrometry (ICP-MS, Perkin-Elmer Plasma 3200). The adsorption amount of Eu(III) was calculated by the difference in the original and finial concentration after adsorption equilibrium.

Preparation and analysis of XPS, EXAFS samples

The samples for XPS and EXAFS analysis were prepared as the similar batch experiments. Briefly, 20 mg of magnetic biochar and 10 mL of 50 mg/L Eu(III) solutions was added into 50 mL polycarbonate centrifuge in glovebox conditions. The pH values and ionic strength were set to 3.0 and 0.01 mol/L, respectively. After reaction equilibrium, the dry solid and wet pastes were collected for the analysis of XPS and EXAFS, respectively. The XPS samples were performed by ESCALAB250 X-ray photoelectron spectrometer (Thermo-VG Scientific, UK) with an Mg–Kα radiation source of 1253.6 eV at 15 kV and 10 mA under 10^{-7} Pa. The binding energies were calibrated with the reference of the C 1s peak at 284.6 eV. The deconvolution of C 1s, O 1s and Eu 3d peaks was conducted using XPSPEAK 41 software. Europium L_{III}-edge EXAFS spectra were collected from BL14W of Shanghai Synchrotron Radiation Facility by Si (111) double crystal monochromator in fluorescence mode. The pre-treatment of EXAFS data was done using Athena program of IFEFFIT 7.0 software, and then Fourier transformed EXAFS

spectra was fitted by Artemis interfaces with an aid of theoretical parameters [36, 37].

Surface complexation modeling

The pH-dependent adsorption and adsorption isotherms of Eu(III) on magnetic biochar was simulated by diffuse layer model of surface complexation modeling with an aid of MINTEQL 2.6 mode [38]. The protonation and deprotonation reactions can be described as Eqs. (1) and (2), respectively:

$$\mathrm{SOH} + \mathrm{H}^{+} = \mathrm{SOH}_2^{+} \log \mathrm{K}^{+} = \log\left(\left[\mathrm{SOH}_2^{+}\right]/([\mathrm{SOH}]^{*}[\mathrm{H}^{+}])\right) \quad (1)$$

$$\mathrm{SOH} = \mathrm{SO}^{-} + \mathrm{H}^{+} \log \mathrm{K}^{-} = \log(([\mathrm{SO}^{-}]^{*}[\mathrm{H}^{+}])/[\mathrm{SOH}]) \quad (2)$$

where SOH refers to the amphoteric reactive sites of magnetic biochar. The values of log K^+ and log K^- were obtained by fitting the titration data of magnetic biochar in the presence of NaCl solutions.

Results and discussion

Characterization

The morphology of magnetic biochar was illustrated by SEM and TEM. As shown by SEM in Fig. 1a, magnetite nanoparticles were uniformly aggregated on the surface of biochar. The biochar networks can efficiently prevent the magnetite nanoparticles from aggregations. The SEM results indicated the improved the surface area and mass transfer for Eu(III) adsorption. As shown by high resolution TEM in Fig. 1b, the particle sizes of these nanoparticles ranged from 50 to 100 nm. In addition, these octahedral nanoparticles were achieved on the surface of biochar matrix due to the porous structure. As shown by fast Fourier transmission (FFT) analysis in Fig. 1b, the distances of main lattice lines were consistent with the distance of (311) plane of magnetite, indicating the formation of as-prepared magnetite nanoparticle. The further evidence was provided by XRD analysis. As shown in Fig. 1c, the diffraction peaks at 2θ = 30.2, 35.5, 43.2, 57.3 and 62.9° were indexed to (220), (311), (400), (511) and (440) planes of magnetite, indicating that magnetic biochar was successfully synthesized by one-step pyrolysis method [33]. The $FeCl_2$-biomass was initially pyrolysed to $Fe(OH)_3$/FeO(OH) and/or Fe_3O_4 at high temperature. Alternatively, the FeO(OH) can be further reduced to Fe3O4 by amorphous carbon during pyrolysis process. These reactions could be described by Eqs. (3)–(6):

$$6\mathrm{FeCl_2} + 6\mathrm{H_2O} + \mathrm{O_2} = 2\mathrm{Fe_3O_4} + 12\mathrm{HCl} \quad (3)$$

$$4\mathrm{FeCl_2} + 10\mathrm{H_2O} + \mathrm{O_2} = 4\mathrm{Fe(OH)_3} + 8\mathrm{HCl} \quad (4)$$

$$\mathrm{Fe(OH)_3} = \mathrm{FeO(OH)} + \mathrm{H2O} \quad (5)$$

$$12\mathrm{FeO(OH)} + \mathrm{C} = 4\mathrm{Fe_3O_4} + \mathrm{CO_2} + 6\mathrm{H_2O} \quad (6)$$

Figure 1d shows the FT-IR spectra of magnetic biochar. The FT-IR bands at 1735 and 1650 cm^{-1} were attributed to the stretching vibration of carboxyl C=O and aromatic C=C groups, respectively [39]. The FT-IR bands at 3400 and 3202 cm^{-1} were attributed to the vibrations of –OH groups [40]. As expected, FT-IR peak at 585 cm^{-1} was corresponded to the stretching vibration of Fe–O groups [41]. As shown in Table 1, the BET-N_2 surface area of magnetic biochar (126.23 m^2/g) was significantly higher than that of magnetite (72.51 m^2/g), which could be attributed the release of small organic molecules and unconverted compositions of biomass at high pyrolysis temperature. The main contents of biochar were C (59.4%) and O (37.7%), whereas magnetic biochar presented the C (46.4%), Fe(19.4%) and O (31.3%) (Table 1). The characteristic results indicated the magnetic biochar was successfully synthesized by one-step pyrolysis method. The as-prepared magnetic biochar displayed the variety of oxygen-containing functional groups.

Adsorption kinetics

As shown in Fig. 2a, the adsorption of Eu(III) on magnetic biochar increased with increasing reaction time from 0 to 24 h, and then slightly increase of Eu(III) adsorption was observed at reaction time more than 24 h. Additionally, the adsorption of Eu(III) on magnetic biochar was slightly higher than that Eu(III) adsorption on magnetite and biochar. The data of adsorption kinetics were fitted by pseudo-first-order and pseudo-second-order kinetic models. The linear forms of pseudo-first-order and pseudo-second-order kinetic models can be described by Eqs. (7) and (8), respectively:

$$\ln(Q\mathrm{e} - Qt) = \ln Q\mathrm{e} - k_1 t \quad (7)$$

$$t/Qt = 1/\left(k_2 Q\mathrm{e}^2\right) + t/Q\mathrm{e} \quad (8)$$

where Qt and Qe (mg/g) refer to the amount of Eu(III) adsorbed on the adsorbents at time t and equilibrium, respectively. k_1 and k_2 are the corresponding adsorption rate constants of pseudo-first-order and pseudo-second-order model, respectively.

The fitted results and corresponding parameters were showed in Fig. 2a and Table 2, respectively. It is observed that the adsorption kinetics of Eu(III) on magnetite, biochar and magnetic biochar can be satisfactorily simulated by pseudo-second-order model with high correlation

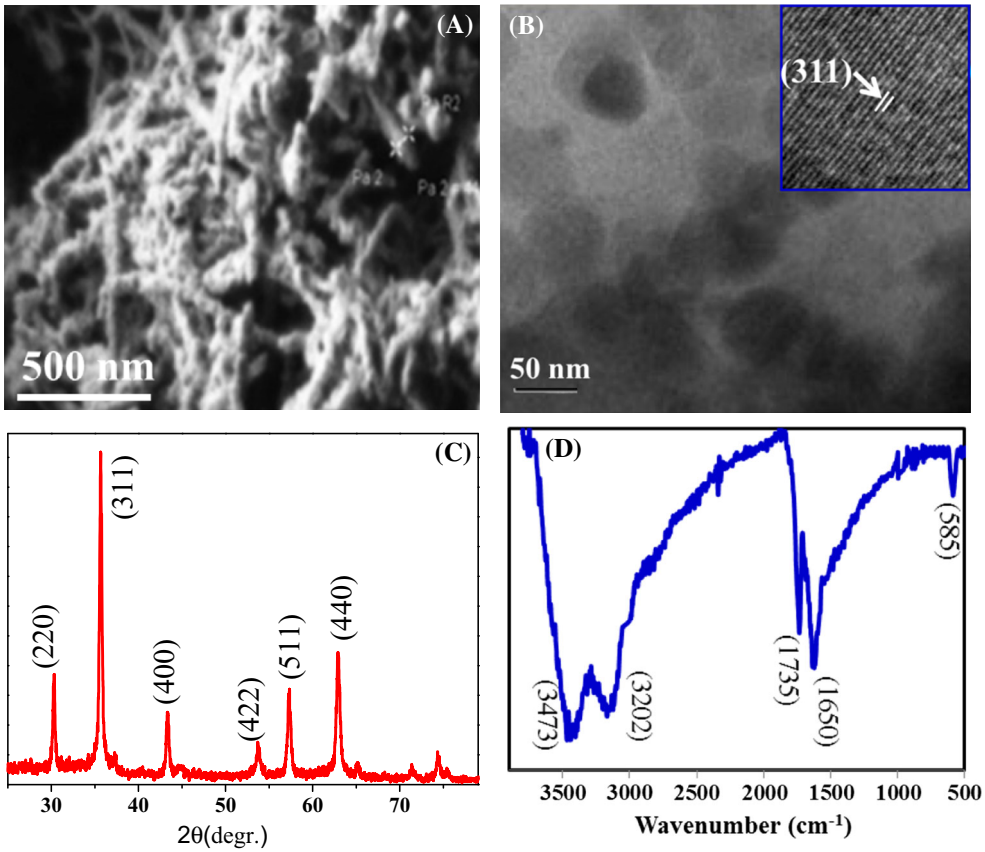

Fig. 1 Characterization of magnetic biochar, **a** SEM; **b** TEM, inset of FFT analysis; **c** XRD; **d** FT-IR

Table 1 The selected properties of magnetic biochar

Contents (%)	Biochar: C(59.4), H(2.3), N(1.4), O(37.7)
	Magnetic biochar: C(46.4), H(1.6), N(1.06), O(31.3), Fe(19.4)
N_2-BET (m^2/g)	Magnetite: 72.51; magnetic biochar: 126.23

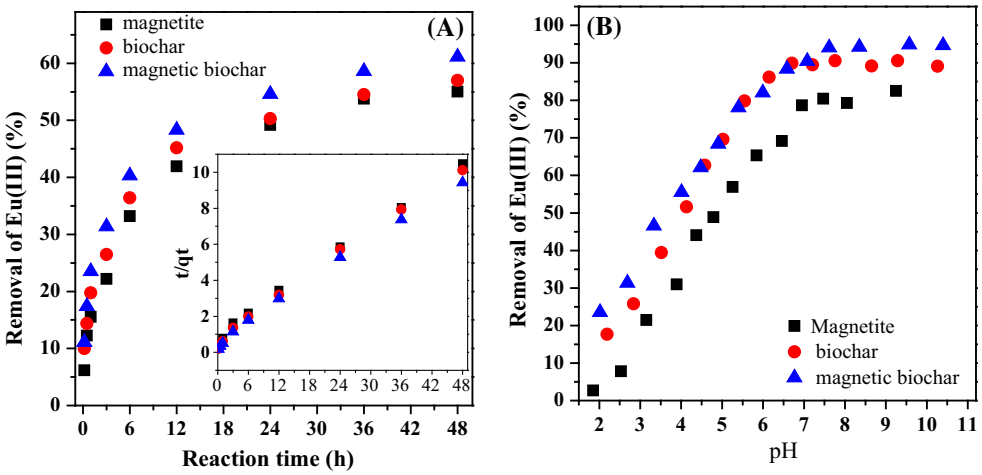

Fig. 2 **a** Adsorption kinetics of Eu(III) on magnetite, biochar and magnetic biochar, $C_{Eu(III)}$ = 10 mg/L, pH 3.0, m/v = 1.2 g/L, T = 293 K; **b** effect of pH on Eu(III) adsorption on magnetite, biochar and magnetic biochar, $C_{Eu(III)}$ = 10 mg/L, m/v = 1.2 g/L, T = 293 K

Table 2 Kinetics parameters of pseudo-first-order and pseudo-second-order model for Eu(III) adsorption on magnetic biochar (1), raw biochar (2) and magnetite (3)

	Pseudo-first-order model			Pseudo-second-order model		
	Qe (mg/g)	k_1 (min^{-1})	R^2	Qe (mg/g)	k_2 (g/(mg min)	R^2
(1)	6.786	0.015	0.8524	4.83	0.0627	0.9947
(2)	6.487	0.0147	0.8421	4.89	0.0792	0.9955
(3)	6.212	0.0161	0.8417	5.21	0.084	0.9961

coefficient ($R^2 > 0.99$) compared to pseudo-first-order model ($R^2 < 0.90$), which were consistent with the previous studies [42–44].

pH effect

Figure 2b shows the effect of pH on Eu(III) adsorption on magnetite, biochar and magnetic biochar. Eu(III) adsorption on three adsorbents significantly increased with increasing pH from 2.0 to 7.0, and then high-level adsorption was observed at pH > 7.0. The increased adsorption of Eu(III) at pH 2.0–7.0 and pH > 7.0 could be attributed to the surface complexation and electrostatic attraction, respectively [13]. The adsorption of Eu(III) on magnetite was significantly lower than that of biochar and magnetic biochar. Eu(III) adsorption on magnetic biochar at pH < 4.0 and > 7.0 was slightly higher than that of biochar, whereas no change in Eu(III) adsorption on magnetic biochar and biochar was observed at pH 4.5–7.0. This results indicated that magnetic nanoparticles and biochar play an important role in Eu(III) adsorption on magnetic biochar at low and near neutral pH, respectively.

Adsorption isotherms and regeneration

Figure 3a shows the adsorption isotherms of Eu(III) on magnetite, biochar and magnetic biochar at pH 3.0 and 293 K. The adsorption of Eu(III) on magnetic biochar was significantly higher than that of magnetite. The data of adsorption isotherms were fitted by Langmuir and Freundlich models. The Langmuir and Freundlich model were described as Eqs. (9) and (10), respectively:

$$\mathrm{qe} = (K \times \mathrm{qmax} \times \mathrm{Ce})/(1 + K \times \mathrm{Ce}) \quad (9)$$

$$\mathrm{qe} = \mathrm{Kf} \times \mathrm{Ce}^{\mathrm{n}} \quad (10)$$

where qmax is the maximum adsorption amount of Eu(III) on magnetic biochar. K (L/mg) and Kf (mg$^{(1-n)}$L^n/g) are the constants of Langmuir and Freundlich model, respectively. The fitted results and corresponding parameters were showed in Fig. 3a and Table 3, respectively. The adsorption of Eu(III) on magnetic biochar, biochar and magnetite can be satisfactorily simulated by Langmuir with high correlation coefficient ($R^2 > 0.995$) compared to Freundlich model ($R^2 < 0.95$). The maximum adsorption capacities of magnetite, biochar and magnetic biochar calculated from Langmuir model at pH 3.0 and 293 K were 88.45, 97.95 and 105.53 mg/g, respectively. These results showed that magnetic biochar can be used as a promising candidate in wastewater treatment to remove radionuclides from aqueous solutions.

Figure 3b shows the regeneration experiments of Eu(III) on magnetic biochar under five recycle times. The maximum adsorption capacities of magnetic biochar decreased from 105.53 mg/g at first time to 91.63 mg/g at fifth time.

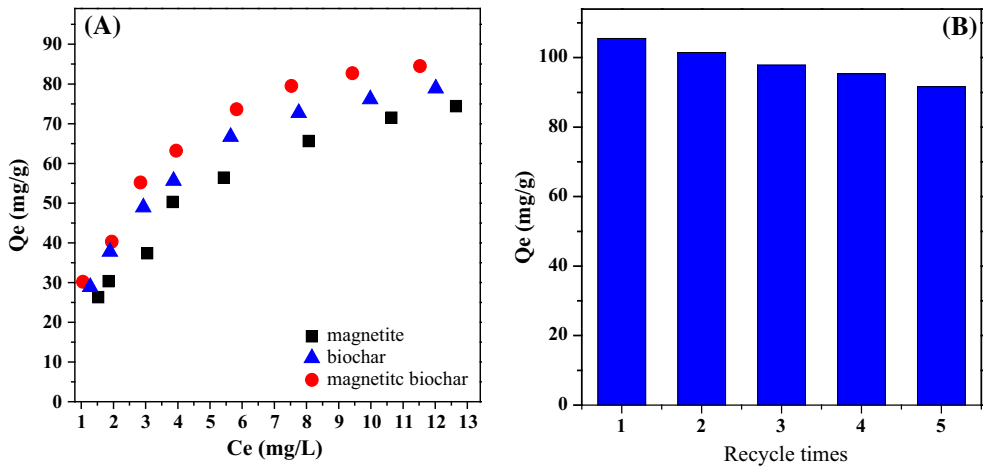

Fig. 3 **a** Adsorption isotherms of Eu(III) on magnetite, biochar and magnetic biochar; **b** regeneration of Eu(III) on magnetic biochar, pH 3.0, m/v = 1.2 g/L, T = 293 K

Table 3 The parameters of Langmuir and Freundlich model for Eu(III) adsorption on magnetic biochar (1), raw biochar (2) and magnetite (3)

	Langmuir model			Freundlich model		
	Q_{max} (mg/g)	K_L (L/mg)	R^2	Ln Q_e	K_F	R^2
(1)	105.53	0.2532	0.9993	3. 374	0.5743	0.9053
(2)	97.95	0.22152	0.9992	3.285	0.6532	0.9056
(3)	88.45	0.1974	0.9997	3.1279	0.6956	0.91545

The regeneration experiments indicated that the adsorption efficiency of magnetic biochar maintained almost unchanged for five recycle times, indicating that the magnetic biochar represented a favorable recycle performance toward Eu(III) removal. The regeneration experiments indicated that magnetic biochar presented the excellent adsorption performance for Eu(III), recyclability and easy recovery.

XPS analysis

Figure 4a and b show the total scans and Eu 3d XPS spectra of magnetic biochar, respectively. As shown in Fig. 4a, the magnetic biochar displayed the C 1s, O 1s and Fe 2p peaks, whereas the Eu 3d peaks was observed for magnetic biochar after Eu(III) adsorption. It is observed that the change in the relative intensities and binding energies of O 1s were observed for magnetic biochar after Eu(III) adsorption, indicating that oxygen- containing functional groups were responsible for highy effective removal of Eu(III) on magnetic biochar [15]. In addition, the relative intensity of Eu 3d at pH 6.5 was significantly higher than that of Eu 3d at pH 3.0, suggesting that the high adsorption of Eu(III) at pH 6.0 was observed, consistent with the pH-dependent adsorption. As shown in Fig. 4b, two peaks of Eu 3d at 1135 and 1165 eV can be attributed to the Eu $3d_{5/2}$ and Eu $3d_{3/2}$, respectively. The results of XPS analysis indicated that magnetic biochar had abundant oxygen-containing functional groups, which was responsible for the Eu(III) adsorption.

EXAFS analysis

Figure 5a and b showed the k^3-weighted Eu(III) EXAFS spectra and the corresponding Fourier transform (FT) data of samples, respectively. The absorption position at $\sim$ 6984.1 eV revealed trivalent Eu in all samples [45]. As shown in Fig. 5a, a single wave frequency of aqueous Eu(III) monotonically decreased amplitude at $k > 3$ Å^{-1}, whereas the evident frequencies of crystalline $Eu(OH)_3$ was observed, which was ascribed to the ordered coordination shell [46]. These observations were attributed to the multiple backscattering paths in the first coordination shell and the higher atomic shells [47]. The broaden oscillation at $k \sim 6.0$ Å^{-1} for magnetic biochar after Eu(III) adsorption pH 3.0 and 6.5 indicated the formation of inner-sphere surface complexes [45]. As shown in Fig. 5b, the bond distances of Eu–O shell for magnetic biochar after Eu(III) adsorption pH 3.0 (2.43 Å) and 6.5 (2.41 Å) were shorter than that of Eu–O shell of aqueous Eu(III) (2.44 Å), whereas these bond distances were slightly larger than that of $Eu(OH)_3$ (2.40 Å) (Table 4). In addition, the occurrence of Eu–C shells for magnatic biochar at pH 3.0 and 6.5 indicated the formation of inner-sphere surface complexation [48]. The FT features at $\sim$ 2.0 Å could be due to the nearest coordination shell of oxygen atoms, which was

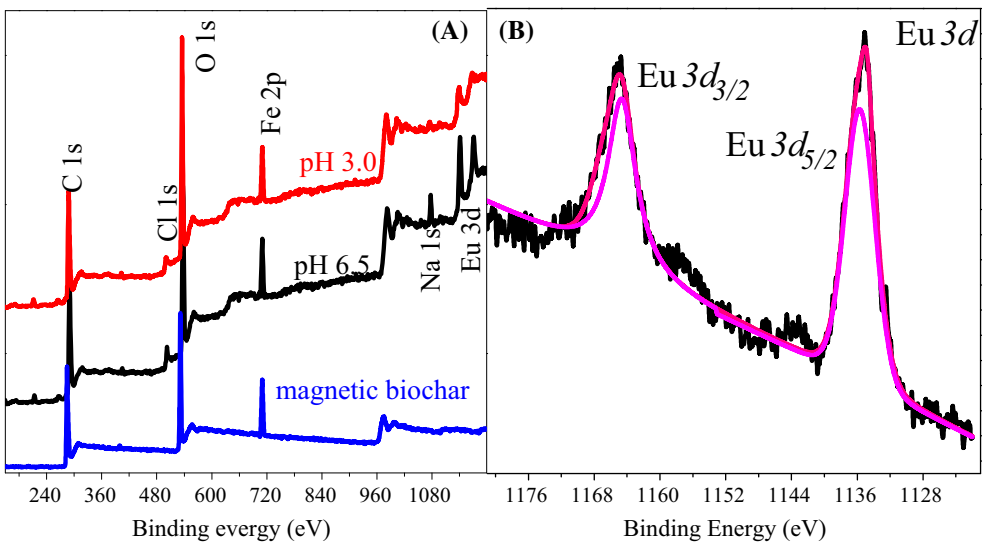

Fig. 4 XPS spectra of magnetic biochar before and after Eu(III) adsorption, **a** total scans; **b** Eu 3d

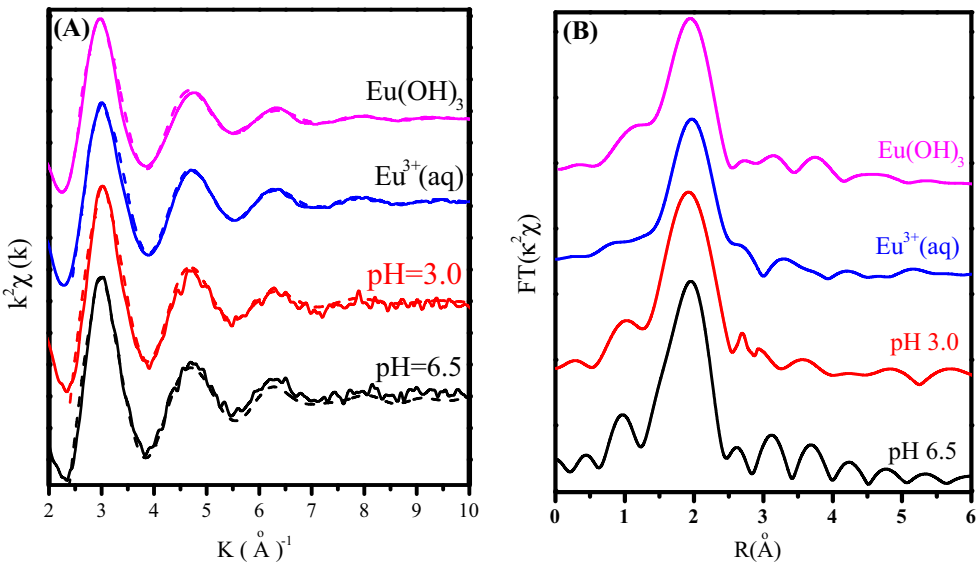

Fig. 5 Eu L_{III}-edge EXAFS spectra (**a**) and corresponding Fourier transforms (**b**) of reference samples and magnetic biochar after Eu(III) adsorption at pH 3.0 and 6.5, $C_{Eu(III)}$ = 10 mg/L, m/v = 1.2 g/L, T = 293 K

Table 4 EXAFS analysis of reference samples and Eu(III) adsorbed on magnetic biochar at Eu L_{III}-Edge, T = 293 K, I = 0.01 mol L^{-1} NaCl

Sample	Shell	R (Å)	CN	σ^2 (Å^2)
$Eu(OH)_3$	Eu–O	2.40 (5)	9.1 (0)	0.0023 (8)
	Eu–Eu	3.65 (4)	1.9 (0)	0.0042 (3)
Eu(aq)	Eu–O	2.44 (3)	8.5 (4)	0.0059 (7)
Magnetic biochar	Eu–O	2.43 (7)	6.7 (0)	0.0024 (6)
pH 3.0	Eu–C	2.32 (8)	4.1 (9)	0.0029 (1)
Magnetic biochar	Eu–O	2.41 (6)	6.0 (4)	0.0026 (8)
pH 6.5	Eu–C	2.311 (2)	4.4 (0)	0.0037 (9)
	Eu–Eu	3.531 (6)	2.4 (8)	0.0032 (1)

R the bond distance, *CN* coordination numbers, σ^2 the Debye–Waller factor

consistent with the adsorption of Eu(III) on calcium silicate hydrates [47]. The coordination numbers of Eu–O shell for magnetic biochar after Eu(III) adsorption at pH 3.0 (CN = 6.7) and 6.5 (CN = 6.0) were significantly lower than that of aqueous Eu(III) (CN = 8.5), which further evidenced the inner-sphere surface complexation. In addition, the occurrence of Eu–Eu shell for magnetic biochar after Eu(III) adsorption at pH 6.5 was similar to the that of Eu–Eu shell of $Eu(OH)_3$ standard, indicating that the adsorbed Eu(III) was gradually formed the surface co-precipitation (e.g., $Eu(OH)_3$ (s)) at high pH conditions. EXAFS results indicated that the adsorption mechanism of Eu(III) and magnetic biochar over wide pH range was inner-sphere surface complexation, whereas the adsorbed Eu(III) was gradually formed the surface co- precipitation at high pH conditions.

Surface complexation modeling

Figure 6a and b show the surface complexation modeling of Eu(III) removal on magnetic biochar at different pH and Eu(III) concentration, respectively. In this study, the double layer model was employed to simulate the adsorption behaviors with an aid of visual MINTEQ mode. The optimized parameters of Eu(III) on magnetic biochar can were summarized in Table 5. As shown in Fig. 6a, the adsorption of Eu(III) on magnetic biochar at different pH conditions can be satisfactorily by double layer model with two inner-sphere surface complexes ($SOEu^{2+}$ and $(SO)_2Eu(OH)_2^-$ species). It is observed that the main adsorbed species was $SOEu^{2+}$ at pH < 4.0, whereas the $(SO)_2Eu(OH)_2^-$ species dominated the Eu(III) adsorption at pH > 5.0. The same optimized parameters were utilized to simulate the data of isothermal adsorption at pH 4.0 (Fig. 6b). Enough interested, the adsorption isotherms of Eu(III) on magnetic biochar was successfully fitted by these two inner-sphere surface complexes derived from the pH-dependent adsorption. The main species was $SOEu^{2+}$ species, which was consistent with the results of pH-dependent adsorption. The results of surface complexation modeling indicated that pH-dependent and isothermal adsorption of Eu(III) on magnetic biochar can be satisfactorily fitted by double layer model with two inner-sphere surface complexes such as $SOEu^{2+}$ and $(SO)_2Eu(OH)_2^-$ species.

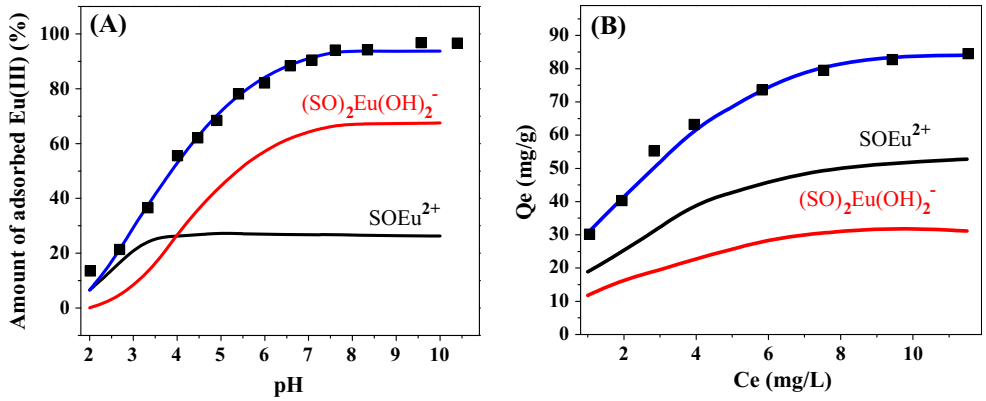

Fig. 6 Surface complexation modeling of Eu(III) adsorption at different pH (**a**) and concentration (**b**) conditions, m/v = 1.2 g/L, T = 293 K

Table 5 Optimized parameters of surface complexation modeling for Eu(III) adsorption on magnetic biochar

Reactions	Log K
Protonation and deprotonation	
$SOH + H^+ = SOH_2^+$	5.3
$SOH = SO^- + H^+$	− 7.5
Surface complexation	
$SOH + Eu^{3+} = SOEu^{2+} + H^+$	2.43
$2SOH + Eu(OH)_2^+ = (SO)_2Eu(OH)_2^- + 2H^+$	− 1.85

Conclusions

Magnetic biochar was successfully synthesized by fast pyrolysis of Fe(II)-preloaded biomass under N_2 condition. The batch adsorption experiments showed that magnetic biochar was effective in enhancing adsorption performance towards Eu(III) compared to magnetite and raw biochar. According to XPS analysis, the high efficient adsorption of Eu(III) on magnetic biochar was attributed to oxygen-containing functional groups. The inner-sphere surface complexation and surface co-precipitation dominated the Eu(III) adsorption on magnetic biochar at low and high pH, respectively. The pH-dependent and isothermal adsorption of Eu(III) on magnetic biochar can be satisfactorily fitted by two inner-sphere surface complexes. These findings offer a new alternative to transform biomass waste into a promising adsorbent for radionuclides removal and further provide mechanistic insights of the interaction between radionuclides and biochar-based nanomaterials.

Acknowledgements Financial support from Natural Science Foundation of China (21577093) and Science and Technology Project of Shaoxing (2014B70041) are acknowledged.

References

1. Chang HS, Buettner SW, Seaman JC, Jaffe PR, van Groos PG, Li D, Peacock AD, Scheckel KG, Kaplan DI (2014) Uranium immobilization in an iron-rich rhizosphere of a native wetland plant from the Savannah River Site under reducing conditions. Environ Sci Technol 48:9270–9278
2. Sun YB, Yang SB, Chen Y, Ding CC, Cheng WC, Wang XK (2015) Adsorption and desorption of U(VI) on functionalized graphene oxides: a combined experimental and theoretical study. Environ Sci Technol 49:4255–4262
3. Rabung T, Pierret MC, Bauer A, Geckeis H, Bradbury MH, Baeyens B (2005) Sorption of Eu(III)/Cm(III) on Ca-montmorillonite and Na-illite. Part 1: batch sorption and time-resolved laser fluorescence spectroscopy experiments. Geochim Cosmochim Acta 69:5393–5402
4. Wang XX, Sun YB, Alsaedi A, Hayat T, Wang XK (2015) Interaction mechanism of Eu(III) with MX-80 bentonite studied by batch, TRLFS and kinetic desorption techniques. Chem Eng J 264:570–576
5. Sun YB, Li JX, Wang XK (2014) The retention of uranium and europium onto sepiolite investigated by macroscopic, spectroscopic and modeling techniques. Geochim Cosmochim Acta 140:621–643
6. Schnurr A, Marsac R, Rabung T, Lutzenkirchen J, Geckeis H (2015) Sorption of Cm(III) and Eu(III) onto clay minerals under saline conditions: batch adsorption, laser-fluorescence spectroscopy and modeling. Geochim Cosmochim Acta 151:192–202
7. Li MX, Sun YB, Liu HB, Chen TH, Hayat T, Alabadi NS, Chen CL (2017) Spectroscopic and modeling investigation of Eu(III)/U(VI) sorption on nanomagnetite from aqueous solutions. ACS Sustain Chem Eng 5:5493–5502
8. Sun YB, Chen CL, Tan XL, Shao DD, Li JX, Zhao GX, Yang SB, Wang Q, Wang XK (2012) Enhanced adsorption of Eu(III) on mesoporous Al_2O_3/expanded graphite composites investigated by macroscopic and microscopic techniques. Dalton Trans 41:13388–13394
9. Rabung T, Geckeis H, Kim JI, Beck HP (1998) Sorption of Eu(III) on a natural hematite: application of a surface complexation model. J Colloid Interface Sci 208:153–161
10. Estes SL, Arai Y, Becker U, Fernando S, Yuan K, Ewing RC, Zhang JM, Shibata T, Powell BA (2013) A self-consistent model describing the thermodynamics of Eu(III) adsorption onto hematite. Geochim Cosmochim Acta 122:430–447
11. Sun YB, Shao DD, Chen CL, Yang SB, Wang XK (2013) Highly efficient enrichment of radionuclides on graphene oxide-supported polyaniline. Environ Sci Technol 47:9904–9910

12. Hu BW, Hu QY, Xu D, Chen CG (2017) Macroscopic and microscopic investigation on adsorption of Sr(II) on sericite. J Mol Liq 225:563–568
13. Sun YB, Wang Q, Chen CL, Tan XL, Wang XK (2012) Interaction between Eu(III) and graphene oxide nanosheets investigated by batch and extended X-ray absorption fine structure spectroscopy and by modeling techniques. Environ Sci Technol 46:6020–6027
14. Xie Y, Helvenston EM, Shuller-Nickles LC, Powell BA (2016) Surface complexation modeling of Eu(III) and U(VI) interactions with graphene oxide. Environ Sci Technol 50:1821–1827
15. Sun YB, Wu Z-Y, Wang XX, Ding CC, Cheng WC, Yu S-H, Wang XK (2016) Macroscopic and microscopic investigation of U(VI) and Eu(III) adsorption on carbonaceous nanofibers. Environ Sci Technol 50:4459–4467
16. Wang XX, Yang SB, Shi WQ, Li JX, Hayat T, Wang XK (2015) Different interaction mechanisms of Eu(III) and Am-243(III) with carbon nanotubes studied by batch, spectroscopy technique and theoretical calculation. Environ Sci Technol 49:11721–11728
17. Liu WJ, Jiang H, Yu HQ (2015) Development of biochar-based functional materials: toward a sustainable platform carbon material. Chem Rev 115:12251–12285
18. Hu QY, Zhu YL, Hu BW, Lu SH, Sheng GD (2018) Mechanistic insights into sequestration of U(VI) toward magnetic biochar: Batch, XPS and EXAFS techniques. J Environ Sci. https://doi.org/10.1016/j.jes.2018.01.013
19. Chen B, Chen Z, Lv S (2011) A novel magnetic biochar efficiently sorbs organic pollutants and phosphate. Bioresour Technol 102:716–723
20. Devi P, Saroha AK (2014) Synthesis of the magnetic biochar composites for use as an adsorbent for the removal of pentachlorophenol from the effluent. Bioresour Technol 169:525–531
21. Dong CD, Chen CW, Hung CM (2017) Synthesis of magnetic biochar from bamboo biomass to activate persulfate for the removal of polycyclic aromatic hydrocarbons in marine sediments. Bioresour Technol 245:188–195
22. Jung KW, Choi BH, Jeong TU, Ahn KH (2016) Facile synthesis of magnetic biochar/Fe3O4 nanocomposites using electro-magnetization technique and its application on the removal of acid orange 7 from aqueous media. Bioresour Technol 220:672–676
23. Devi P, Saroha AK (2015) Simultaneous adsorption and dechlorination of pentachlorophenol from effluent by Ni-ZVI magnetic biochar composites synthesized from paper mill sludge. Chem Eng J 271:195–203
24. Han YT, Cao X, Ouyang X, Sohi SP, Chen JW (2016) Adsorption kinetics of magnetic biochar derived from peanut hull on removal of Cr(VI) from aqueous solution: effects of production conditions and particle size. Chemosphere 145:336–341
25. Wang SY, Tang YK, Li K, Mo YY, Li HF, Gu ZQ (2014) Combined performance of biochar sorption and magnetic separation processes for treatment of chromium-contained electroplating wastewater. Bioresour Technol 174:67–73
26. Zhang MM, Liu YG, Li TT, Xu WH, Zheng BH, Tan XF, Wang H, Guo YM, Guo FY, Wang SF (2015) Chitosan modification of magnetic biochar produced from *Eichhornia crassipes* for enhanced sorption of Cr(VI) from aqueous solution. RSC Adv 5:46955–46964
27. Trakal L, Veselska V, Safarik I, Vitkova M, Cihalova S, Komarek M (2016) Lead and cadmium sorption mechanisms on magnetically modified biochars. Bioresour Technol 203:318–324
28. Yan LL, Kong L, Qu Z, Lo L, Shen GQ (2015) Magnetic biochar decorated with ZnS nanocrytals for Pb(II) removal. ACS Sustain Chem Eng 3:125–132
29. Yap MW, Mubarak NM, Sahu JN, Abdullah EC (2017) Microwave induced synthesis of magnetic biochar from agricultural biomass for removal of lead and cadmium from wastewater. J Ind Eng Chem 45:287–295
30. Wang SS, Gao B, Zimmerman AR, Li YC, Ma L, Harris WG, Migliaccio KW (2015) Removal of arsenic by magnetic biochar prepared from pinewood and natural hematite. Bioresour Technol 175:391–395
31. Zhang M, Gao B, Varnoosfaderani S, Hebard A, Yao Y, Inyang M (2013) Preparation and characterization of a novel magnetic biochar for arsenic removal. Bioresour Technol 130:457–462
32. Liu SB, Huang BY, Chai LY, Liu YG, Zeng GM, Wang X, Zeng W, Shang MR, Deng JQ, Zhou Z (2017) Enhancement of As(V) adsorption from aqueous solution by a magnetic chitosan/biochar composite. RSC Adv 7:10891–10900
33. Hu BW, Hu QY, Xu D, Chen CG (2017) The adsorption of U(VI) on carbonaceous nanofibers: a combined batch, EXAFS and modeling techniques. Sep Purif Technol 175:140–146
34. Ding CC, Cheng WC, Sun YB, Wang XK (2015) Novel fungus-Fe_3O_4 bio-nanocomposites as high performance adsorbents for the removal of radionuclides. J Hazard Mater 295:127–137
35. Hu BW, Chen GH, Hu J, Huang CC, Sheng J, Sheng GD, Ma JY, Huang YY (2017) Macroscopic and spectroscopic studies of the enhanced scavenging of Cr(VI) and Se(VI) from water by titanate nanotube anchored nanoscale zero-valent iron. J Hazard Mater 336:214–221
36. Newville M (2001) EXAFS analysis using FEFF and FEFFIT. J Synchrotron Rad 8:96–100
37. Hu BW, Ye F, Ren XM, Zhao DL, Sheng GD, Li H, Ma JY, Wang XK, Huang YY (2016) X-ray absorption fine structure study of enhanced sequestration of U(VI) and Se(IV) by montmorillonite decorated zerovalent iron nanoparticles. Environ Sci 3:1460–1472
38. Gustafsson JP (2009) A windows version of MINTEQ. http://www.lwr.kth.se/English/ OurSOrware/vminteq/index.htm
39. Sun YB, Lu SH, Wang XX, Xu C, Li JX, Chen CL, Chen J, Hayat T, Alsaedi A, Alharbi NS, Wang XK (2017) Plasam-facilitated synthesis of amidoxime/carbon nanofiber hybrids for effective enrichment of ^{238}U(VI) and ^{241}Am(III). Environ Sci Technol 51:12274–12282
40. Qiu MQ, Wang M, Zhao QZ, Hu BW, Zhu YL (2018) XANES and EXAFS investigation of uranium incorporation on nZVI in the presence of phosphate. Chemosphere 201:764–771
41. Jin ZX, Wang XX, Sun YB, Ai YJ, Wang XK (2015) Adsorption of 4-n-nonylphenol and bisphenol-A on magnetic reduced graphene oxides: a combined experimental and theoretical studies. Environ Sci Technol 49:9168–9175
42. Liu HB, Li MX, Chen TH, Chen CL, Alharbi NS, Hayat T, Sun YB (2017) New synthesis of nZVI/C composites as an efficient adsorbents for the uptake of U(VI) from aqueous solutions. Environ Sci Technol 51:9227–9234
43. Ding CC, Cheng WC, Sun YB, Wang XK (2015) Effects of *Bacillus subtilis* on the reduction of U(VI) by nano-Fe^0. Geochim Cosmochim Acta 165:86–107
44. Sun YB, Zhang R, Ding CC, Wang XX, Cheng WC, Chen CL, Wang XK (2016) Adsorption of U(VI) on sericite in the presence of *Bacillus subtilis*: a combined batch, EXAFS and modeling techniques. Geochim Cosmochim Acta 180:51–65
45. Hu BW, Qu MQ, Sun YB, Sheng GD, Hu J, Ma JY (2017) Decontamination of Sr(II) adsorption on magnetic polyanaline/graphene oxide composites: evidence from experimental, spectroscopic, and modeling investigation. ACS Sustain Chem Eng 5:6924–6931
46. Sheng GD, Yang PJ, Hu QY, Li H, Ren XM, Hu BW, Wang XK, Huang YY (2016) New insights into the primary roles of diatomite in the enhanced sequestration of UO22+ by zerovalent iron nanoparticles: an advanced approach utilizing XPS and EXAFS. Appl Catal B 193:189–197

47. Hu BW, Hu QY, Chen CG, Sun YB, Xu D, Sheng GD (2017) New insights into Th(IV) speciation on sepiolite: evidence for EXAFS and modeling investigation. Chem Eng J 322:66–72

48. Fan QH, Tan XL, Li JX, Wang XK, Wu WS, Montavon G (2009) Sorption of Eu(III) on attapulgite studied by batch, XPS, and EXAFS techniques. Environ Sci Technol 43:5776–5782